A 2-D Differential Surface Admittance Operator for Combined Magnetic and Dielectric Contrast

Dries Bosman, Martijn Huynen, Daniël De Zutter, Hendrik Rogier and Dries Vande Ginste

Ghent University – imec, Department of Information Technology, IDlab, QUEST/EM Group, Ghent, Belgium

Abstract

In this paper, we present a novel technique to accurately model scattering phenomena at two-dimensional circular and rectangular structures consisting of arbitrary homogeneous materials, including magnetic media in particular. The proposed formalism utilizes a differential surface admittance operator, which invokes a single source equivalence theorem to replace the inside material by its surrounding medium, while introducing an equivalent surface current density. The arbitrary magnetic contrast can be combined with an arbitrary electrical conductivity. As such, the skin effect is rigorously taken into account, making our method ideally suited for broadband modeling of good conductors as well. It is demonstrated that an appropriate choice of the basis functions for the discretized problem is critical to obtain a convergent result when magnetic contrast is introduced. The method is analytically validated for the case of a circular cylinder and additional numerical results illustrate the correctness of the technique for (combinations of) rectangular cylinders, through comparison with a Poggio-Miller-Chan-Harrington-Wu-Tsai approach, a volume integral equation method and a commercial solver.

Keywords: Differential surface admittance operator, magnetic materials, boundary integral equations, electromagnetic scattering

1. Introduction

Electronic devices are prevalent in today's information society and the ever more stringent demands in terms of complexity, processing speed and compactness constitute considerable challenges for the design engineers. On the hardware level, the increasing clock frequencies and the steady strive for miniaturization cause concern when it comes to, e.g., electromagnetic compatibility (EMC) and signal and power integrity (SI/PI). Consequently, accurate solvers are of paramount importance to provide reliable predictions during the development of the next generation of technological appliances.

In this context, with structures that can no longer be regarded as electrically small, full-wave electromagnetic solvers are required. These models capture the wave nature of the pertinent fields and rigorously solve Maxwell's equations in a numerical fashion. One can distinguish various families of solvers, of which the finite difference, finite element and integral equation methods are the most notable.

The discretization of the object under consideration can be performed by means of a volumetric scheme, such as the finite element method (FEM) or a surface-based one, as applied in boundary integral equation (BIE) formulations. The latter group of methods allows to solely discretize the surface area. Consequently, the number of unknowns in the system to be solved is greatly reduced, although a dense system matrix must be tolerated. A well-known example, applicable to piecewise homogeneous scatterers, is the Poggio-Miller-Chan-Harrington-Wu-Tsai (PMCHWT) method [1].

When the scattering object is made of highly conductive materials, solving the problem remains, however, quite challenging. These difficulties may be attributed to a particularly strenuous phenomenon to model, viz., the skin effect, which causes the fields in a good conductor to reside ever closer to its surface at increasing frequencies. Various methods have been devised to tackle the skin effect, both in FEM [2, 3] and BIE [4, 5] techniques. Often, they introduce additional relations between the tangential electric and magnetic fields on the surface. The surface impedance is such a commonly used principle, specifying a local relationship on the boundary of the considered object, thus eliminating the so-called 'internal field problem'. A notable example in this category is based on the Leontovich boundary condition [6]. A generalization to a more global relationship, using volume integral equations (VIE), was presented in [7]. However, these techniques all suffer from inaccuracies and approximations that limit their applicability [8].

Another method, specifically tailored to this type of problems, employs the so-called differential surface admittance (DSA) operator. It was first presented in [9] as a concept to accurately and efficiently characterize circular and rectangular two-dimensional (2-D) good conductors over a wide frequency range, thus rigorously capturing the skin effect. This is achieved by recasting the problem at hand into an equivalent one, where the material of the conductor is replaced by its surrounding medium and an equivalent surface current density is introduced to maintain the outside fields of the original configuration. Consequently, cumbersome numerical integrations involving the Green's function inside the good conductor are avoided [10]. After its conception in 2005, the 2-D DSA formalism was utilized to effectively model scattering problems [11] and to accurately determine transmission line parameters, also in the presence of semiconductors [12]. As relatively high numbers of Dirichlet eigenfunctions in the conductor's cross-section are required to construct the DSA operator, a restriction to canonical shapes was preferred. However, this limitation was circumvented in [13], presenting an alternative route that allowed to incorporate triangular structures. The technique was later extended to three-dimensional electromagnetic scattering and interconnect modeling, including cylindrical and cuboid structures [14, 15, 16]. Although the aforementioned incarnations of the DSA technique are able to accurately and efficiently model a wide variety of homogeneous materials, they are all limited to nonmagnetic media only.

Several formalisms invoking an equivalent surface current density for 2-D structures with, in principle, arbitrary material properties have been proposed by Patel et al. The initial focus of their work was directed toward the calculation of the series impedance of power cables with a circular cross-section embedded in a homogeneous medium [17]. Subsequently, this method was extended to support tubular conductors [18], multi-cable configurations in circular cavities [19] and layered background media [20]. A generalization to conductors with arbitrary cross-section was presented in [21]. This later culminated in a method applicable to 3-D scattering from dielectric objects [22]. However, in all of these formulations, numerical issues may arise. It is well-known that modeling of penetrable objects with high magnetic or dielectric contrast is very challenging [23]. Additionally, as stated before, dealing with the Green's functions inside a conductive medium is complicated, in particular in the case of a strongly developed skin effect [10]. Techniques to alleviate these limitations, which are also present in traditional, well-established BIE methods, will inevitably lead to an increased computational cost [24].

Here, we propose a novel, modified DSA approach that is able to tackle broadband 2-D scattering problems involving dielectric, magnetic and highly conductive materials alike, without relying on Green's functions inside the considered objects. Moreover, this formulation does not break down for high magnetic contrasts, since only the background medium is involved in the solution of the outside problem, while preconditioning of the system matrix would otherwise be required [25].

The remainder of this paper is structured as follows. In Section 2, the DSA operator for circular and rectangular cylinders is constructed using a Fourier series approach. The discretization scheme is conceived such that the convergence of the solution is guaranteed and that the employed basis functions allow for a convenient integration in the BIE formalism detailed in Section 3. In particular, it is shown that the choice of piecewise linear basis functions for the tangential electric field is indispensable, while simple pulse-shaped basis functions for the equivalent differential surface current density ensure a straightforward formulation and solution of the BIE. Once the theoretical aspects of the proposed technique are fully developed, we turn our attention to numerical results in Section 4. First, the numerical implementation is validated for circular cylinders by comparison with the analytical solution. Next, we illustrate the proper convergence of the technique for rectangular cylinders. To conclude the results section, the correctness, efficiency and versatility of our method are further explored by comparing the results for scattering problems with the solutions obtained by means of the PMCHWT method and a VIE approach, alongside the outcome of a commercial solver.

2. Construction of the Differential Surface Admittance Operator

Assume an $e^{j\omega t}$ dependence for time-harmonic transverse magnetic[1] (TM) polarized electromagnetic fields $(\boldsymbol{e}_{\mathrm{inc}}, \boldsymbol{h}_{\mathrm{inc}})$ incident on a cylinder with cross section $\mathcal{S}$, boundary $\mathcal{C}$ and outward pointing normal vector $\hat{\boldsymbol{n}}$, as shown in Fig. 1a. The longitudinal dimension of the cylinder is aligned along the z-direction. Hence, in this TM context, the electric fields are z-oriented. The scatterer consists of an isotropic and homogeneous material characterized by its permittivity ϵ_{i}, permeability μ_{i} and conductivity σ_{i}, with corresponding wavenumber k_{i}. It is surrounded by a background medium with wavenumber k_{e} and constitutive parameters ϵ_{e}, μ_{e} and σ_{e}. A scattered electromagnetic field $(\boldsymbol{e}_{\mathrm{sc}}, \boldsymbol{h}_{\mathrm{sc}})$ and fields $(\boldsymbol{e}_{\mathrm{i}}, \boldsymbol{h}_{\mathrm{i}})$ inside $\mathcal{S}$ ensue, satisfying the boundary conditions imposed by Maxwell's equations. Efficient numerical modeling of the scattered fields originating from $\mathcal{S}$ is possible by first applying the single source equivalence theorem, i.e., we apply Love's theorem [26], where we choose the equivalent magnetic current density to vanish and allow arbitrary (nonzero) fields $(\boldsymbol{e}'_{\mathrm{i}}, \boldsymbol{h}'_{\mathrm{i}})$ within the cylinder. This creates the situation depicted in Fig. 1b, where the inner medium of $\mathcal{S}$ is replaced by the outside medium, provided an as yet unknown current density $\boldsymbol{j}_{\mathrm{s}}$ is introduced on the boundary $\mathcal{C}$.

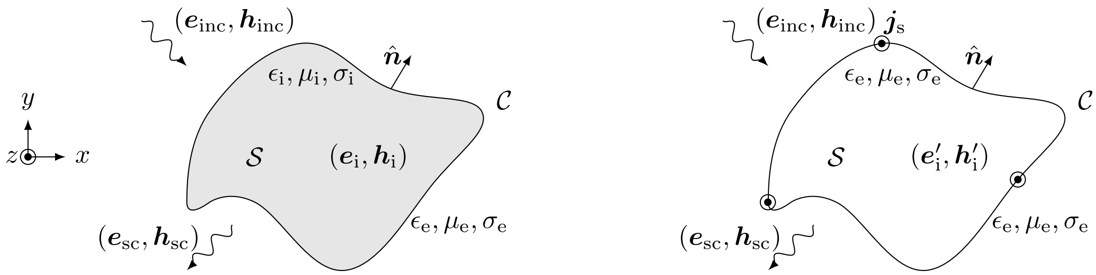

(a) Original problem

(b) Equivalent problem

Figure 1: Illustration of the single source equivalence theorem.

At the boundary $\mathcal{C}$, we can now state that:

$$\boldsymbol{j}_{\mathrm{s}} = \hat{\boldsymbol{n}} \times (\boldsymbol{h}_{\mathrm{i}} - \boldsymbol{h}'_{\mathrm{i}}), \tag{1}$$

$$\hat{\boldsymbol{n}} \times \boldsymbol{e}_{\mathrm{i}} = \hat{\boldsymbol{n}} \times \boldsymbol{e}'_{\mathrm{i}}. \tag{2}$$

It should be noted that the quantities $(\boldsymbol{e}'_{\mathrm{i}}, \boldsymbol{h}'_{\mathrm{i}})$ do not represent real physical fields inside $\mathcal{S}$. Nonetheless, on the boundary $\mathcal{C}$, and only there, we have in our TM case that $\boldsymbol{e}_{\mathrm{i}} = \boldsymbol{e}'_{\mathrm{i}} \triangleq \boldsymbol{e} = e_z \hat{\boldsymbol{z}}$, where, again, it should be noted that $\boldsymbol{e}_{\mathrm{i}}$ and $\boldsymbol{e}'_{\mathrm{i}}$ are z-oriented.

To determine the unknown current density $\boldsymbol{j}_{\mathrm{s}}$ we invoke the Poincaré-Steklov operator $\mathcal{P}$, which expresses the rotated tangential magnetic field $\hat{\boldsymbol{n}} \times \boldsymbol{h}$ in any point on the circumference $\mathcal{C}$ in terms of the tangential electric field $\boldsymbol{e}$ everywhere on $\mathcal{C}$. For Fig. 1a, this yields

$$\hat{\boldsymbol{n}} \times \boldsymbol{h}_{\mathrm{i}} = \mathcal{P}\boldsymbol{e}, \tag{3}$$

while for the situation shown in Fig. 1b, we can write

$$\hat{\boldsymbol{n}} \times \boldsymbol{h}'_{\mathrm{i}} = \mathcal{P}'\boldsymbol{e}. \tag{4}$$

By subtracting (4) from (3) and utilizing (1), we finally obtain the following result for $\boldsymbol{j}_{\mathrm{s}}$:

$$\boldsymbol{j}_{\mathrm{s}} = \hat{\boldsymbol{n}} \times (\boldsymbol{h}_{\mathrm{i}} - \boldsymbol{h}'_{\mathrm{i}}) = (\mathcal{P} - \mathcal{P}')\boldsymbol{e} \triangleq \mathcal{Y}\boldsymbol{e}, \tag{5}$$

where $\mathcal{Y}$ is the sought-after DSA operator.

[1] We first consider the TM case as this proves to be the most problematic in terms of convergence when magnetic contrast is present. Moreover, the transverse electric (TE) case can be solved by simply performing the appropriate substitutions and considering it as the dual case, given the fact that dielectric and magnetic contrast are taken into account simultaneously by our method.

2.1. Circular Region

The DSA formalism is now applied to a circular cylinder of radius a aligned along the z-axis. For this cylinder, the 2-D TM scattering of a plane wave can of course be solved entirely analytically. Hence, this example is ideally suited not only to prove that the novel, modified DSA technique proposed in this paper is correct, but also to demonstrate why a modification is needed in the presence of magnetic contrast. More specifically, we will show that, when magnetic materials are present, a well-chosen set of basis functions for the tangential electric field and the equivalent differential surface current density is critical for the convergence of the discretized DSA operator. Although this transition to local basis functions is clearly not strictly necessary for the case of the circular cylinder, we choose to adopt this approach to thoroughly validate the proposed formalism and to provide insight into its properties.

The usual cylindrical coordinates (r, ϕ, z) are introduced. The tangential electric field e_z is expanded into piecewise linear (rooftop) basis functions, with center angles ϕ_p and opening angle δ:

$$e_z \approx \sum_{p=1}^{P} v_p t_p(\phi), \tag{6}$$

with

$$t_p(\phi) = \begin{cases} \frac{2}{\delta}\left[\phi - \left(\phi_p - \frac{\delta}{2}\right)\right], & \phi_p - \frac{\delta}{2} \leqslant \phi \leqslant \phi_p \\ \frac{2}{\delta}\left[\left(\phi_p + \frac{\delta}{2}\right) - \phi\right], & \phi_p \leqslant \phi \leqslant \phi_p + \frac{\delta}{2} \\ 0, & \text{otherwise.} \end{cases} \tag{7}$$

Note that this differs from the expansion into pulse basis functions as, e.g., used in [9]. For the surface current density $\boldsymbol{j}_{\mathrm{s}} = j_{s,z}\hat{\boldsymbol{z}}$, on the other hand, we still resort to constant (pulse) basis functions of opening angle Δ, centered around ϕ_m:

$$j_{s,z} \approx \sum_{m=1}^{M} i_m b_m(\phi), \tag{8}$$

with

$$b_m(\phi) = \begin{cases} 1, & \phi_m - \frac{\Delta}{2} \leqslant \phi \leqslant \phi_m + \frac{\Delta}{2} \\ 0, & \text{otherwise.} \end{cases} \tag{9}$$

Now, we substitute (6) and (8) into (5) and test (5) with the constant basis functions $b_{m'}$ as defined in (9), yielding

$$\sum_{m=1}^{M} i_m \int\limits_{\mathcal{C}} b_{m'}(\phi) b_m(\phi) a \,\mathrm{d}\phi = \sum_{p=1}^{P} v_p \int\limits_{\mathcal{C}} b_{m'}(\phi) \mathcal{Y} t_p(\phi') a \,\mathrm{d}\phi \,, \tag{10}$$

or, in matrix form:

$$\boldsymbol{G}^{(2)} \boldsymbol{i} = \boldsymbol{Y} \boldsymbol{v}. \tag{11}$$

The expansion coefficients v_p are collected in the $P \times 1$ column vector $\boldsymbol{v}$, while the $M \times 1$ column vector $\boldsymbol{i}$ contains the expansion coefficients i_m. The elements of the $M \times M$ Gram matrix $\boldsymbol{G}^{(2)}$ and the $M \times P$ admittance matrix $\boldsymbol{Y}$ are given by

$$G_{ij}^{(2)} = \int\limits_{\mathcal{C}} b_i(\phi) b_j(\phi) a \,\mathrm{d}\phi \,, \tag{12}$$

$$Y_{ij} = \int\limits_{\mathcal{C}} b_i(\phi) \mathcal{Y} t_j(\phi') a \,\mathrm{d}\phi \,. \tag{13}$$

The circumference of the circle is subdivided into M equal intervals subtending an angle $\Delta = 2\pi/M$, such that the constant basis functions have midpoints $\phi_m = \Delta/2 + (m-1)\Delta$, with $m \in \{1, 2, \ldots, M\}$. Next, we construct an equal number (i.e., $P = M$) of piecewise linear basis functions with span $\delta = 2\Delta$ and midpoints

$\phi_p = p\Delta$, where $p \in \{1, 2, \ldots, P\}$. Remark that basis function t_P wraps around to the first interval. The elements of the Gram matrix in (12) are then evaluated as

$$G^{(2)}_{ij} = \begin{cases} a\Delta, & i = j \\ 0, & i \neq j. \end{cases} \tag{14}$$

To determine the elements of $\boldsymbol{Y}$, an analytical Fourier series approach is utilized. Consequently, exact results are obtained, apart from the discretization errors and the approximation introduced by truncation of the Fourier series in the numerical implementation. First, the Fourier series expansions of the basis functions b_m and t_p are required:

$$b_m = \sum_n \beta_{mn} e^{jn\phi} \qquad \text{with } \beta_{mn} = \begin{cases} e^{-jn\phi_m} \dfrac{\sin(n\Delta/2)}{n\pi}, & n \neq 0 \\ \dfrac{\Delta}{2\pi}, & n = 0, \end{cases} \tag{15}$$

$$t_p = \sum_n \tau_{pn} e^{jn\phi} \qquad \text{with } \tau_{pn} = \begin{cases} e^{-jn\phi_p} \dfrac{4\sin^2(n\delta/4)}{n^2\pi\delta}, & n \neq 0 \\ \dfrac{\delta}{4\pi}, & n = 0. \end{cases} \tag{16}$$

Likewise, we introduce the Fourier series expansions of the tangential electric field e_z and the differential surface current density $j_{s,z}$:

$$e_z = \sum_n \alpha_n e^{jn\phi}, \tag{17}$$

$$j_{s,z} = \sum_n \iota_n e^{jn\phi}. \tag{18}$$

In Appendix A.1, it is proven that a Fourier component α_n of e_z results in a corresponding differential surface current density coefficient given by

$$\iota_n = \Upsilon_n \alpha_n = \left[\frac{k_\mathrm{i}}{j\omega\mu_\mathrm{i}} \frac{J'_n(k_\mathrm{i}a)}{J_n(k_\mathrm{i}a)} - \frac{k_\mathrm{e}}{j\omega\mu_\mathrm{e}} \frac{J'_n(k_\mathrm{e}a)}{J_n(k_\mathrm{e}a)} \right] \alpha_n, \tag{19}$$

with J_n the n-th order Bessel function. To introduce the Fourier domain DSA operator Υ_n into (11), we determine expressions relating the coefficients α_n and v_p, on the one hand, and ι_n and i_m, on the other hand. Starting from (6), we first determine the Fourier coefficients α_n of e_z:

$$\frac{1}{2\pi} \sum_{p=1}^{P} v_p \int_0^{2\pi} t_p(\phi) e^{-jn\phi} \,\mathrm{d}\phi = \sum_{p=1}^{P} \tau_{pn} v_p = \alpha_n. \tag{20}$$

Next, we test both expansions (8) and (18) with a constant basis function $b_{m'}$, to find

$$\sum_{m=1}^{M} i_m \int_{\mathcal{C}} b_{m'}(\phi) b_m(\phi) a \,\mathrm{d}\phi = \sum_n \iota_n \int_{\mathcal{C}} b_{m'}(\phi) e^{jn\phi} a \,\mathrm{d}\phi \tag{21}$$

$$\Longleftrightarrow \sum_{m=1}^{M} G^{(2)}_{m'm} i_m = 2\pi a \sum_n \beta^*_{m'n} \iota_n. \tag{22}$$

Subsequently, (19), (20) and (22) are combined, yielding

$$\sum_{m=1}^{M} G^{(2)}_{m'm} i_m = 2\pi a \sum_{p=1}^{P} \sum_n \beta^*_{m'n} \Upsilon_n \tau_{pn} v_p. \tag{23}$$

Identifying with (11), we finally obtain a closed-form expression of the DSA matrix elements:

$$Y_{ij} = 2\pi a \sum_n \beta^*_{in} \Upsilon_n \tau_{jn}. \tag{24}$$

We now investigate the convergence of the series (24) for magnetic media. In Appendix A.2, it is demonstrated that the asymptotic behavior of the ratio between the Bessel function and its derivative for large order n is given by

$$\lim_{n\to\infty} \frac{J_n'(z)}{J_n(z)} = \frac{n}{z} + \mathcal{O}\left(\frac{1}{n}\right). \tag{25}$$

Employing (15), (16) and (19), we observe that the terms of (24) exhibit the following proportionality for large values of $|n|$:

$$Y_{ijn} \propto e^{jn(\phi_j - \phi_i)} \frac{1}{|n|} \frac{1}{n^2} |n| \left[\left(\frac{1}{\mu_\mathrm{i}} - \frac{1}{\mu_\mathrm{e}} \right) + \mathcal{O}\left(\frac{1}{n^2}\right) \right]. \tag{26}$$

Consequently, the absolute values of these terms decrease as $1/n^2$, and the sum in (24) converges. Note that this behavior is a result of the presence of the Fourier coefficients of the piecewise *linear* basis function t_p (7), which decrease as $1/n^2$ (see (7)). If, instead, we had expanded the tangential electric field into constant basis functions as well, as in the original approach in [9], then the factor $1/n^2$ in (26) would be replaced by $1/|n|$. In that case, the series would become divergent. It is important to note that in [9] no magnetic contrast was included, and it can be seen from (26) that the convergence problem always disappears when $\mu_\mathrm{i} = \mu_\mathrm{e}$, in which case employing constant pulse basis functions poses no issue. However, in the case with magnetic contrast, the proposed modification with linear basis functions is essential.

2.2. Rectangular Region

The technique to construct the 2-D TM DSA operator for magnetic materials is now adopted for a rectangular cylinder with its longitudinal dimension extending in the z-direction and its sides with lengths l_x and l_y parallel to the other two coordinate axes, as illustrated in Fig. 2. The sides are numbered 1 through 4, counterclockwise, starting with the bottom one. Once more, the tangential electric field e_z is represented by piecewise *linear* basis functions and an equal number of constant basis functions models the equivalent differential surface current density $j_{s,z}$. We again resort to a Fourier series approach and apply the superposition principle, i.e., we set e_z equal to zero on all but one of the sides of the rectangle and determine the corresponding tangential magnetic field. By reiterating this approach for each of the four sides and summing the resulting contributions, we obtain the complete picture. This way, a Poincaré-Steklov operator is determined for both situations in Fig. 1, and their difference eventually constitutes the DSA operator for rectangular cylinders.

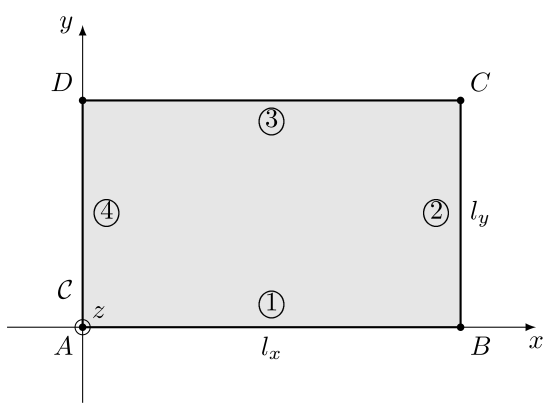

Figure 2: Rectangular cylinder extending along the z-axis with transversal dimensions $l_x \times l_y$.

Let $e_z^{(2)} = e_z^{(3)} = e_z^{(4)} = 0$, while $e_z^{(1)} \neq 0$, with the superindex referring to the sides. We expand the z-oriented electric field on side 1 (or, more specifically, its odd periodic extension) in a Fourier series, taking the boundary conditions imposed by $e_z^{(2)} = e_z^{(4)} = 0$ into account:

$$e_z^{(1)} = \sum_n \alpha_n(y) \sin \lambda_x x, \qquad \text{with } \lambda_x = \frac{n\pi}{l_x}. \tag{27}$$

For the original problem of Fig. 1a, this electric field inside the medium satisfies the Helmholtz equation:

$$\nabla^2 e_z^{(1)} + k_\mathrm{i}^2 e_z^{(1)} = 0, \tag{28}$$

which evaluates to

$$\sum_n \left[\frac{\mathrm{d}^2\alpha_n}{\mathrm{d}y^2} + \left(k_\mathrm{i}^2 - \lambda_x^2\right)\alpha_n\right]\sin\lambda_x x = 0. \tag{29}$$

To obtain (29), we interchanged the summation over n and the differentiation with respect to x and y, which is allowed, as shown in Appendix C. Taking into account that $e_z^{(3)} = 0$ on side 3 ($y = l_y$), we then find

$$\alpha_n = p_n \sin\kappa_{x,\mathrm{i}}(y - l_y) \qquad \text{with } \kappa_{x,\mathrm{i}}^2 = k_\mathrm{i}^2 - \lambda_x^2. \tag{30}$$

Now, we derive the corresponding tangential magnetic fields through

$$j\omega\mu_\mathrm{i}\boldsymbol{h}_\mathrm{t} = \hat{\boldsymbol{z}} \times \boldsymbol{\nabla} e_z, \tag{31}$$

or

$$j\omega\mu_\mathrm{i} h_x = -\frac{\partial e_z^{(1)}}{\partial y} \qquad \text{on sides 1 and 3,} \tag{32}$$

$$j\omega\mu_\mathrm{i} h_y = \frac{\partial e_z^{(1)}}{\partial x} \qquad \text{on sides 2 and 4.} \tag{33}$$

We substitute (30) into (27) and, using the above expressions (32) and (33) for h_x and h_y, we find

$$h_x = -\frac{1}{j\omega\mu_\mathrm{i}}\sum_n p_n\kappa_{x,\mathrm{i}}\cos\kappa_{x,\mathrm{i}}(y - l_y)\sin\lambda_x x \qquad \text{on sides 1 and 3,} \tag{34}$$

$$h_y = \frac{1}{j\omega\mu_\mathrm{i}}\sum_n p_n\lambda_x\sin\kappa_{x,\mathrm{i}}(y - l_y)\cos\lambda_x x \qquad \text{on sides 2 and 4.} \tag{35}$$

On side 1 ($y = 0$), we have that $e_z^{(1)} = -\sum_n p_n \sin\kappa_{x,\mathrm{i}} l_y \sin\lambda_x x$. We choose p_n such that $-p_n\sin\kappa_{x,\mathrm{i}} l_y = 1$ and, elaborating (34) and (35), we determine the contribution of each individual Fourier basis function $e_{zn}^{(1)} = \sin\lambda_x x$ on side 1 to the tangential magnetic field on each of the four sides, leading to

$$h_{xn}^{(1)} = \frac{\kappa_{x,\mathrm{i}}}{j\omega\mu_\mathrm{i}}\cot\kappa_{x,\mathrm{i}} l_y \sin\lambda_x x, \qquad \text{for side 1 } (y = 0), \tag{36}$$

$$h_{xn}^{(3)} = \frac{\kappa_{x,\mathrm{i}}}{j\omega\mu_\mathrm{i}}\csc\kappa_{x,\mathrm{i}} l_y \sin\lambda_x x, \qquad \text{for side 3 } (y = l_y), \tag{37}$$

$$h_{yn}^{(2)} = -\frac{1}{j\omega\mu_\mathrm{i}}(-1)^n\lambda_x\frac{\sin\kappa_{x,\mathrm{i}}(y - l_y)}{\sin\kappa_{x,\mathrm{i}} l_y}, \qquad \text{for side 2 } (x = l_x), \tag{38}$$

$$h_{yn}^{(4)} = -\frac{1}{j\omega\mu_\mathrm{i}}\lambda_x\frac{\sin\kappa_{x,\mathrm{i}}(y - l_y)}{\sin\kappa_{x,\mathrm{i}} l_y}, \qquad \text{for side 4 } (x = 0). \tag{39}$$

Repeating the above calculations for the equivalent problem of Fig. 1b and using (5), the final contributions of a unit Fourier component of the tangential electric field on side 1 to the equivalent differential surface current density on all four sides can now be summarized as

$$j_{s,z}^{(1)} = \frac{1}{j\omega}\left(\frac{\kappa_{x,\mathrm{i}}}{\mu_\mathrm{i}}\cot\kappa_{x,\mathrm{i}} l_y - \frac{\kappa_{x,\mathrm{e}}}{\mu_\mathrm{e}}\cot\kappa_{x,\mathrm{e}} l_y\right)\sin\lambda_x x = \Upsilon_{11}\sin\lambda_x x, \tag{40}$$

$$j_{s,z}^{(3)} = -\frac{1}{j\omega}\left(\frac{\kappa_{x,\mathrm{i}}}{\mu_\mathrm{i}}\csc\kappa_{x,\mathrm{i}} l_y - \frac{\kappa_{x,\mathrm{e}}}{\mu_\mathrm{e}}\csc\kappa_{x,\mathrm{e}} l_y\right)\sin\lambda_x x = \Upsilon_{31}\sin\lambda_x x, \tag{41}$$

$$j_{s,z}^{(2)} = -\frac{1}{j\omega}(-1)^n\lambda_x\left(\frac{\sin\kappa_{x,\mathrm{i}}(y - l_y)}{\mu_\mathrm{i}\sin\kappa_{x,\mathrm{i}} l_y} - \frac{\sin\kappa_{x,\mathrm{e}}(y - l_y)}{\mu_\mathrm{e}\sin\kappa_{x,\mathrm{e}} l_y}\right) = \Upsilon_{21}^\mathrm{i}\sin\kappa_{x,\mathrm{i}}(y - l_y) - \Upsilon_{21}^\mathrm{e}\sin\kappa_{x,\mathrm{e}}(y - l_y), \tag{42}$$

$$j_{s,z}^{(4)} = \frac{1}{j\omega}\lambda_x\left(\frac{\sin\kappa_{x,\mathrm{i}}(y - l_y)}{\mu_\mathrm{i}\sin\kappa_{x,\mathrm{i}} l_y} - \frac{\sin\kappa_{x,\mathrm{e}}(y - l_y)}{\mu_\mathrm{e}\sin\kappa_{x,\mathrm{e}} l_y}\right) = \Upsilon_{41}^\mathrm{i}\sin\kappa_{x,\mathrm{i}}(y - l_y) - \Upsilon_{41}^\mathrm{e}\sin\kappa_{x,\mathrm{e}}(y - l_y). \tag{43}$$

Above, we expanded $e_z^{(1)}$ into the Fourier functions $\sin \lambda_x x$. We repeat this for $e_z^{(3)}$, while for $e_z^{(2)}$ and $e_z^{(4)}$ we use the corresponding Fourier functions $\sin \lambda_y y$ (with $\lambda_y = n\pi/l_y$). This procedure can be summarized symbolically as

$$e_z = \sum_{\nu} \alpha_\nu f_\nu(c), \tag{44}$$

where ν represents the Fourier index on either of the four sides and $f_\nu(c)$ is one of the Fourier basis functions, corresponding to the considered side. For each Fourier function, a differential surface current density contribution similar to (40)–(43) arises. We represent all of these contributions symbolically as

$$j_{s,z} = \sum_{\nu} \iota_\nu g_\nu(c). \tag{45}$$

For $e_z^{(1)}$, the $g_\nu(c)$ functions are $\sin \lambda_x x$ on sides 1 and 3 (see (40) and (41)). For sides 2 and 4 we need two functions, viz., $\sin \kappa_{x,\mathrm{i}}(y - l_y)$ and $\sin \kappa_{x,\mathrm{e}}(y - l_y)$ (see (42) and (43)). Of course, similar contributions arise for $e_z^{(2)}$, $e_z^{(3)}$ and $e_z^{(4)}$. By collecting the expansion coefficients α_ν and ι_ν in vectors $\boldsymbol{\alpha}$ and $\boldsymbol{\iota}$, and the admittances $\Upsilon_{ij}^{\mathrm{a}}$ (with $i, j \in \{1, 2, 3, 4\}$ and $\mathrm{a} \in \{\mathrm{i}, \mathrm{e}, \varnothing\}$) in matrix $\boldsymbol{\Upsilon}$, we can write

$$\boldsymbol{\iota} = \boldsymbol{\Upsilon}\boldsymbol{\alpha}. \tag{46}$$

As for the circular cylinder, we represent e_z and $j_{s,z}$ as

$$e_z \approx \sum_{p=1}^{P} v_p t_p(c), \tag{47}$$

$$j_{s,z} \approx \sum_{m=1}^{M} i_m b_m(c), \tag{48}$$

where $t_p(c)$ and $b_m(c)$ are again linear rooftop and constant pulse basis functions, resp. For the rectangular cylinder, the former are defined as

$$t_p(c) = \begin{cases} \dfrac{2}{\delta}\left[c - \left(c_p - \dfrac{\delta}{2}\right)\right], & c_p - \dfrac{\delta}{2} \leqslant c \leqslant c_p \\ \dfrac{2}{\delta}\left[\left(c_p + \dfrac{\delta}{2}\right) - c\right], & c_p \leqslant c \leqslant c_p + \dfrac{\delta}{2} \\ 0, & \text{otherwise,} \end{cases} \tag{49}$$

while the latter are now given by

$$b_m(c) = \begin{cases} 1, & c_m - \dfrac{\Delta}{2} \leqslant c \leqslant c_m + \dfrac{\Delta}{2} \\ 0, & \text{otherwise.} \end{cases} \tag{50}$$

The width and midpoints of the pulse basis functions (50) become $\Delta = l_c/M_c$ and $c_m = \Delta/2 + (m-1)\Delta$, with $m \in \{1, 2, \ldots, M_c\}$. In these expressions c represents x on the horizontal sides and y on the vertical ones, supporting M_x and M_y pulse basis functions, resp. For the definition (49) of the piecewise linear basis functions, we obtain $\delta = 2l_c/(M_c + 1)$ and $c_p = p\delta/2$, with $p \in \{1, 2, \ldots, P_c\}$. We choose $M_c = P_c$, with $c \in \{x, y\}$, such that $M = 2(M_x + M_y) = 2(P_x + P_y) = P$.

To retrieve the relations between the tangential electric field expressed in piecewise linear basis functions and the equivalent differential surface current density expanded into constant basis functions, we proceed in a similar manner as for the circular cylinder. First, we equate both expansions of e_z, i.e., (44) and (47), and test both sides with the Fourier basis functions $f_{\nu'}(c)$:

$$\sum_{\nu=1}^{N} \alpha_\nu \int_{\mathcal{C}} f_{\nu'}(c) f_\nu(c)\,\mathrm{d}c = \sum_{p=1}^{P} v_p \int_{\mathcal{C}} f_{\nu'}(c) t_p(c)\,\mathrm{d}c\,, \tag{51}$$

or, in matrix form:

$$\boldsymbol{D}\boldsymbol{\alpha} = \boldsymbol{M}^{(1)}\boldsymbol{v}, \tag{52}$$

where $\boldsymbol{D}$ is a diagonal scaling matrix and $\boldsymbol{M}^{(1)}$ is a transformation matrix linking the two types of expansions for e_z. For the equivalent differential surface current density, we equate (45) and (48), and test both sides of the equation with a constant pulse basis function:

$$\sum_{\nu=1}^{N} \iota_\nu \int\limits_{\mathcal{C}} b_{m'}(c) g_\nu(c)\,\mathrm{d}c = \sum_{p=1}^{M} i_m \int\limits_{\mathcal{C}} b_{m'}(c) b_m(c)\,\mathrm{d}c\,, \tag{53}$$

yielding the following matrix equation:

$$\boldsymbol{M}^{(2)}\boldsymbol{\iota} = \boldsymbol{G}^{(2)}\boldsymbol{i}, \tag{54}$$

where $\boldsymbol{M}^{(2)}$ is similar to $\boldsymbol{M}^{(1)}$, but now for $j_{s,z}$, and $\boldsymbol{G}^{(2)}$ is a Gram matrix. Collecting the results of (46), (52) and (54), we finally obtain

$$\boldsymbol{G}^{(2)}\boldsymbol{i} = \boldsymbol{M}^{(2)}\boldsymbol{\Upsilon}\boldsymbol{D}^{-1}\boldsymbol{M}^{(1)}\boldsymbol{v} = \boldsymbol{Y}\boldsymbol{v}. \tag{55}$$

Comparing this result to (11) and (24) for a circular cylinder, we observe a very similar structure, where the transformation matrices $\boldsymbol{M}^{(1)}$ and $\boldsymbol{M}^{(2)}$ assume the role of the basis function Fourier coefficients τ and β, resp., while the scaling matrix $\boldsymbol{D}^{-1}$ corresponds to the factor $2\pi a$.

For the cylinder, the behavior of Y_{ijn} for large n (26) clearly shows why rooftop expansion functions for the tangential electric field are required to ensure convergence in the case of magnetic contrast. Let us now, e.g., take a look at Υ_{11} in (40) for $n \to +\infty$. It is easily shown that

$$\lim_{n\to+\infty} \Upsilon_{11} = \frac{1}{j\omega}\left[\left(\frac{1}{\mu_\mathrm{i}} - \frac{1}{\mu_\mathrm{e}}\right) + \mathcal{O}\left(\frac{1}{n^2}\right)\right]\frac{n\pi}{l_x}. \tag{56}$$

This is precisely the same behavior as Υ_n in (19), with a replaced by l_x/π. Consequently, the factors $1/|n|$ and $1/n^2$ appearing in (26), stemming from the Fourier transforms of b_m and t_p, resp., are needed again to make the series convergent. These factors are incorporated in $\boldsymbol{M}^{(2)}$ and $\boldsymbol{M}^{(1)}$.

3. Boundary Integral Equation Formulation

Equipped with expressions for the DSA operator, we are now ready to tackle the outside problem. In a 2-D TM plane wave scattering context, the longitudinal electric field induced by a longitudinal current density (here, the equivalent differential surface current density) in a homogeneous medium, as depicted in Fig. 1b, can be expressed as

$$e_{z,\mathrm{sc}}(\boldsymbol{r}) = j\omega\mu_\mathrm{e} \int\limits_{\mathcal{C}} G(k_\mathrm{e}|\boldsymbol{r}-\boldsymbol{r}'|) j_{s,z}(\boldsymbol{r}')\,\mathrm{d}c(\boldsymbol{r}')\,, \tag{57}$$

where the 2-D Green's function is given by

$$G(k_\mathrm{e}|\boldsymbol{r}-\boldsymbol{r}'|) = \frac{j}{4} H_0^{(2)}(k_\mathrm{e}|\boldsymbol{r}-\boldsymbol{r}'|) \tag{58}$$

and $H_0^{(2)}$ is the zeroth-order Hankel function of the second kind. The total electric field is found by summing the incident and scattered electric fields:

$$e_z = e_{z,\mathrm{inc}} + e_{z,\mathrm{sc}}, \tag{59}$$

which, on the boundary of the cylinder, can be linked to the equivalent differential surface current density by invoking the DSA operator.

3.1. Circular Region

Keeping in mind the discretization we introduced for circular cylinders, in (6) and (8), we test (59) with the piecewise constant basis functions $b_{m'}$ to obtain

$$\sum_{p=1}^{P} v_p \int_{\mathcal{C}} b_{m'}(\phi) t_p(\phi) a \, \mathrm{d}\phi = \int_{\mathcal{C}} b_{m'}(\phi) e_{z,\mathrm{inc}}(\boldsymbol{r}) a \, \mathrm{d}\phi + j\omega\mu_{\mathrm{e}} \sum_{m=1}^{M} i_m \int_{\mathcal{C}} \int_{\mathcal{C}'} G(k_{\mathrm{e}}|\boldsymbol{r} - \boldsymbol{r}'|) b_{m'}(\phi) b_m(\phi') a^2 \, \mathrm{d}\phi' \, \mathrm{d}\phi \,, \tag{60}$$

yielding the following matrix equation:

$$\boldsymbol{G}^{(1)} \boldsymbol{v} = \boldsymbol{p} + j\omega\mu_{\mathrm{e}} \boldsymbol{A} \boldsymbol{i}. \tag{61}$$

Substituting (11) into (61) gives

$$\boldsymbol{G}^{(1)} \boldsymbol{Y}^{-1} \boldsymbol{G}^{(2)} \boldsymbol{i} = \boldsymbol{p} + j\omega\mu_{\mathrm{e}} \boldsymbol{A} \boldsymbol{i}, \tag{62}$$

which we solve for the unknown expansion coefficients $\boldsymbol{i}$. Given the particular basis function configuration we introduced earlier, the elements of the $M \times P$ Gram matrix $\boldsymbol{G}^{(1)}$ are

$$G_{ij}^{(1)} = \int_{\mathcal{C}} b_i(\phi) t_j(\phi) a \, \mathrm{d}\phi = \begin{cases} \dfrac{a\Delta}{2}, & j = i - 1 \text{ or } j = i \\ 0, & \text{otherwise.} \end{cases} \tag{63}$$

For the elements of $\boldsymbol{A}$, the double integral is transformed by expanding the Green's function along the circumference $r = a$ as follows:

$$\frac{j}{4} H_0^{(2)}(k_{\mathrm{e}}|\boldsymbol{r} - \boldsymbol{r}'|) = \frac{j}{4} \sum_n J_n(k_{\mathrm{e}} a) H_n^{(2)}(k_{\mathrm{e}} a) e^{jn(\phi - \phi')}. \tag{64}$$

Since the Hankel function is piecewise smooth, it is allowed to perform term-by-term integration, such that

$$A_{ij} = \frac{ja^2}{4} \sum_n J_n(k_{\mathrm{e}} a) H_n^{(2)}(k_{\mathrm{e}} a) \int_{\mathcal{C}} b_i(\phi) e^{jn\phi} \, \mathrm{d}\phi \int_{\mathcal{C}'} b_j(\phi') e^{-jn\phi'} \, \mathrm{d}\phi' = j\pi^2 a^2 \sum_n J_n(k_{\mathrm{e}} a) H_n^{(2)}(k_{\mathrm{e}} a) \beta_{in}^* \beta_{jn}. \tag{65}$$

Finally, for an excitation by a unit TM polarized plane wave incident along $\hat{\boldsymbol{u}}_{\mathrm{i}} = \hat{\boldsymbol{x}}$, using Bessel's integral, we find the following Fourier expansion:

$$e_{z,\mathrm{inc}} = e^{-jk_{\mathrm{e}} \hat{\boldsymbol{u}}_{\mathrm{i}} \cdot \boldsymbol{r}} = e^{-jk_{\mathrm{e}} x} = e^{-jk_{\mathrm{e}} r \cos\phi} = \sum_n j^{-n} J_n(k_{\mathrm{e}} r) e^{jn\phi}, \tag{66}$$

such that, along the circumference (for $r = a$), the elements of the excitation vector $\boldsymbol{p}$ read

$$p_i = a \sum_n j^{-n} J_n(k_{\mathrm{e}} a) \int_{\mathcal{C}} b_i(\phi) e^{jn\phi} \, \mathrm{d}\phi = 2\pi a \sum_n j^{-n} J_n(k_{\mathrm{e}} a) \beta_{in}^*. \tag{67}$$

3.2. Rectangular Region

For a rectangular cylinder, we proceed in a very similar fashion, yet the elements of $\boldsymbol{A}$ and $\boldsymbol{p}$ are determined by numerical integration, rather than via a Fourier series expansion. In our numerical implementation, special care has been taken to properly evaluate the (nearly-singular) integrals corresponding to the self- and neighbor patch cases [27]. We find

$$A_{ij} = \int_{\mathcal{C}} \int_{\mathcal{C}'} G(k_{\mathrm{e}}|\boldsymbol{r} - \boldsymbol{r}'|) b_i(c) b_j(c') \, \mathrm{d}c' \, \mathrm{d}c \approx \sum_{k=1}^{K} \sum_{l=1}^{L} w_k w_l' G\left(k_{\mathrm{e}}|\boldsymbol{r}_k - \boldsymbol{r}_l'|\right), \tag{68}$$

$$p_i = \int_{\mathcal{C}} b_i(c) e_{z,\mathrm{inc}}(\boldsymbol{r}) \, \mathrm{d}c \approx \sum_{k=1}^{K} w_k e_{z,\mathrm{inc}}(\boldsymbol{r}_k), \tag{69}$$

where $(\boldsymbol{r}_k, w_k)$ and $(\boldsymbol{r}'_l, w'_l)$ are the nodes and weights of two K- and L-point Gauss-Legendre quadrature rules, resp.

Similarly to (63) and (12), the elements of the Gram matrices $\boldsymbol{G}^{(1)}$ and $\boldsymbol{G}^{(2)}$ for the rectangular cylinder are given by

$$G_{ij}^{(1)} = \int\limits_{\mathcal{C}} b_i(c) t_j(c) \,\mathrm{d}c \qquad \text{and} \qquad G_{ij}^{(2)} = \int\limits_{\mathcal{C}} b_i(c) b_j(c) \,\mathrm{d}c \,. \tag{70}$$

4. Numerical Results

4.1. Circular Region

From (6), (8), (15)–(18) we easily derive the following numerical approximations for the Fourier coefficients of the tangential electric field and the equivalent differential surface current density:

$$\alpha_n \approx \sum_{p=1}^{P} \tau_{pn} v_p \qquad \text{and} \qquad \iota_n \approx \sum_{m=1}^{M} \beta_{mn} i_m, \tag{71}$$

while their analytical counterparts $\tilde{\alpha}_n$ and $\tilde{\iota}_n$ are derived in Appendix B. A comparison between both sets for an example configuration is provided in Fig. 3, where a circular cylinder with radius $a = 3\,\mathrm{cm}$, exhibiting material properties $\epsilon_\mathrm{r} = 5$, $\mu_\mathrm{r} = 10$ and $\sigma = 0$ at a frequency of $10\,\mathrm{GHz}$ is considered. The cylinder is illuminated by a plane wave of the form (66). The number of basis functions was set to $M = P = 201$ and only the Fourier coefficients with positive indices are shown because of symmetry. It can be observed that the numerical results match the analytical prediction very well up to Fourier index $n = 27$, beyond which the magnitude of the analytically determined coefficients continues to decrease, while their numerically calculated counterparts reach a plateau, owing to the limited machine precision and rounding errors. Nonetheless, given the very low magnitude of these Fourier coefficients with $n > 27$, the overall accuracy of the method is not adversely affected, as can be observed from the corresponding plots of the tangential electric field e_z (at $r = a$) and equivalent differential surface current density $j_{s,z}$ in Fig. 4. As a final validation, we change the material properties of the cylinder to those of a carbon steel with $\epsilon_\mathrm{r} = 1$, $\mu_\mathrm{r} = 1000$ and $\sigma = 5.8 \times 10^6\,\mathrm{S/m}$. In this case with a highly conductive medium and elevated magnetic contrast, the numerically calculated and analytically determined results for e_z and $j_{s,z}$ agree very well once more, as demonstrated in Fig. 5.

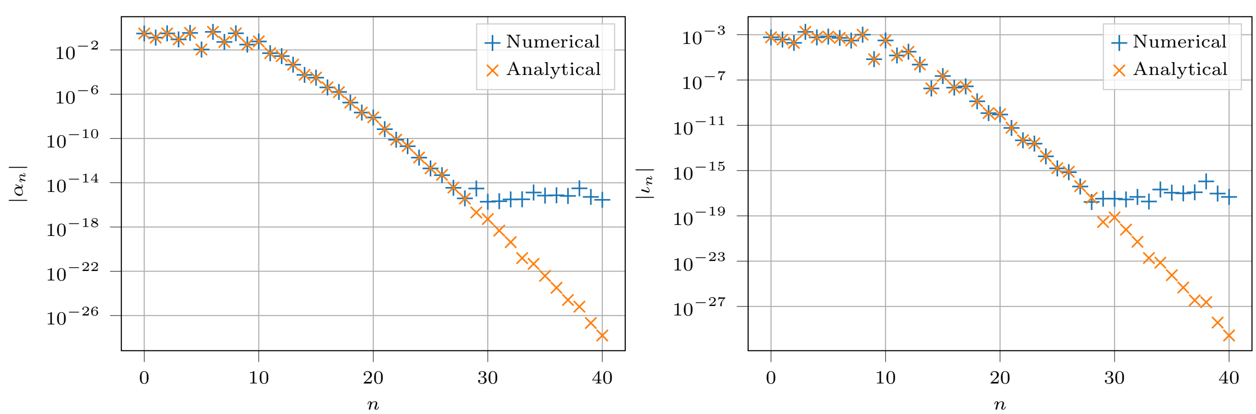

(a) Tangential electric field Fourier coefficients

(b) Equivalent differential surface current density Fourier coefficients

Figure 3: Numerically calculated and analytically determined magnitude of the Fourier coefficients of the tangential electric field and the equivalent differential surface current density for a circular cylinder with radius $a = 3\,\mathrm{cm}$ and material properties $\epsilon_\mathrm{r} = 5$, $\mu_\mathrm{r} = 10$ and $\sigma = 0$, at a frequency of $10\,\mathrm{GHz}$.

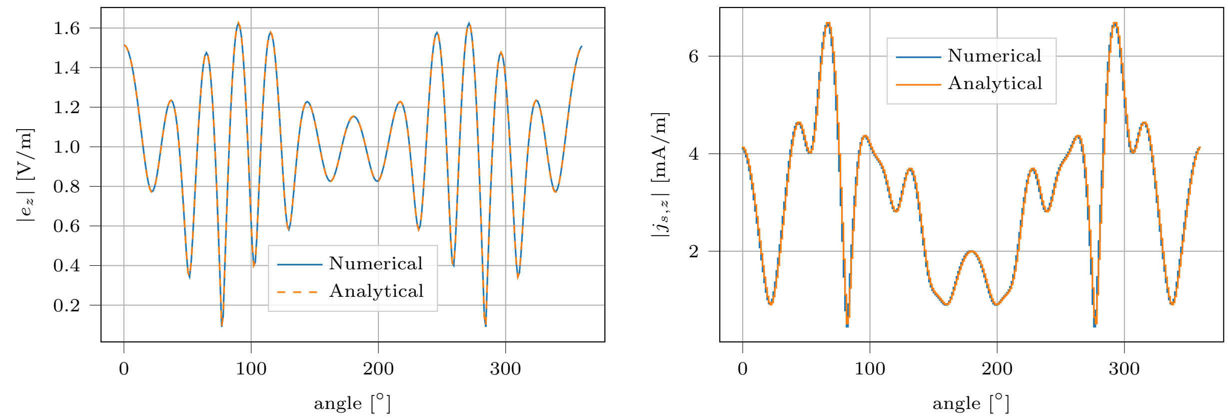

(a) Tangential electric field

(b) Equivalent differential surface current density

Figure 4: Numerically calculated and analytically determined magnitudes of the tangential electric field and the equivalent differential surface current density at the boundary of a circular cylinder with radius $a = 3\,\mathrm{cm}$ and material properties $\epsilon_\mathrm{r} = 5$, $\mu_\mathrm{r} = 10$ and $\sigma = 0$, at a frequency of 10 GHz.

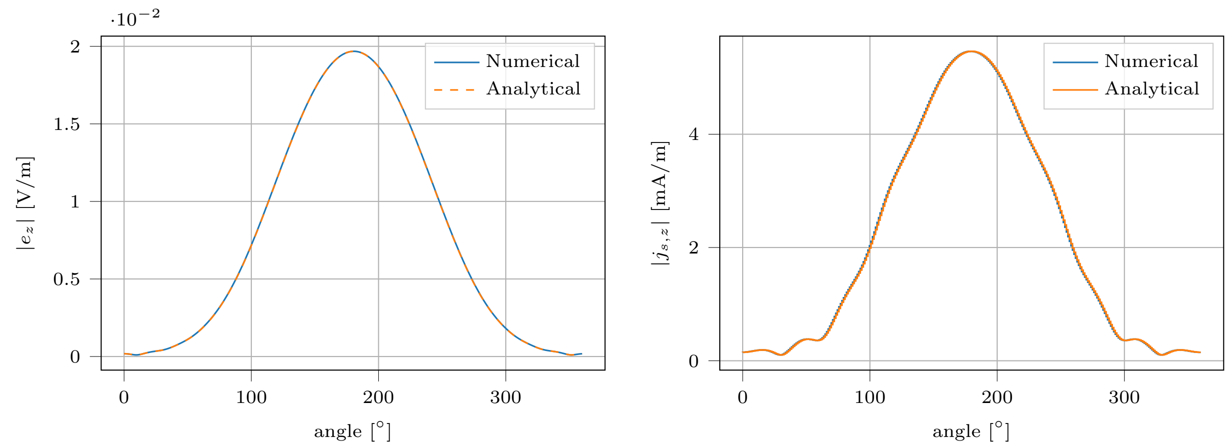

(a) Tangential electric field

(b) Equivalent differential surface current density

Figure 5: Numerically calculated and analytically determined magnitudes of the tangential electric field and the equivalent differential surface current density at the boundary of a circular cylinder with radius $a = 3\,\mathrm{cm}$ and material properties $\epsilon_\mathrm{r} = 1$, $\mu_\mathrm{r} = 1000$ and $\sigma = 5.8 \times 10^6\,\mathrm{S/m}$, at a frequency of 10 GHz.

4.2. Rectangular Region

We consider a $3\,\mathrm{cm} \times 2\,\mathrm{cm}$ rectangular cylinder at 10 GHz, with its horizontal and vertical sides discretized into 45 and 30 segments, resp., relative permittivity $\epsilon_\mathrm{r} = 5$ and varying relative permeability $\mu_\mathrm{r} \in \{1, 10, 100, 1000\}$. To support our statements on the criticality of selecting appropriate basis functions, we study two basis function configurations: expanding both the equivalent differential surface current density $j_{s,z}$ and the tangential electric field e_z in pulse basis functions, or invoking rooftop basis functions for e_z, as proposed in this paper. The absolute values of three elements of the admittance matrix $\boldsymbol{Y}$ are presented in Fig. 6, as a function of the number of sine functions in the Fourier series expansion of the tangential electric field. These three elements Y_{ii} are situated on the diagonal of $\boldsymbol{Y}$ and correspond to the bottom left corner ($i = 1$), the middle of side 1 ($i = 23$) and the middle of side 2 ($i = 61$), resp. In absence of magnetic contrast ($\mu_\mathrm{r} = 1$), the values of the admittance matrix elements converge for either of the two considered basis function configurations. One can, however, clearly observe the divergent behavior when magnetic contrast is introduced, in case the method employing pulse basis functions for e_z is selected (Fig. 6a), while the formalism presented in this paper still produces correct results (Fig. 6b).

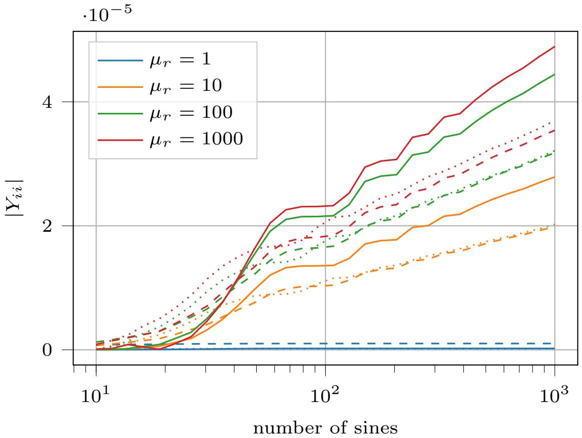

(a) Pulse basis functions

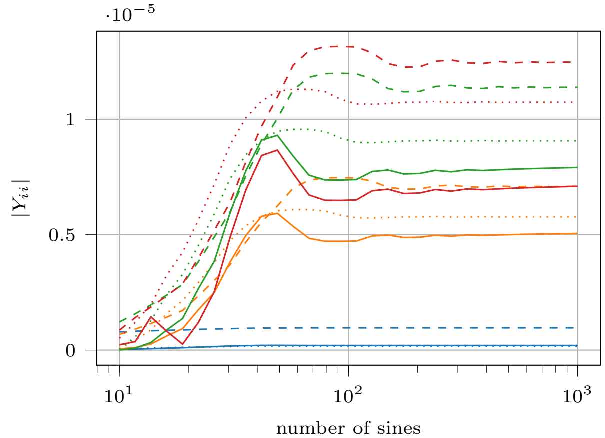

(b) Rooftop basis functions

Figure 6: Convergence of three diagonal admittance matrix elements corresponding to the bottom left corner (solid line), the middle of side 1 (dashed) and the middle of side 2 (dotted) for a 3 cm × 2 cm rectangular cylinder at 10 GHz, with relative permittivity $\epsilon_{\mathrm{r}} = 5$, varying relative permeability μ_{r}, and two basis function configurations for the tangential electric field.

In Fig. 7, we compare the echo width or backscattering cross-section of two rectangular cylinders under illumination by a TM polarized plane wave as determined by means of two techniques: the proposed method and a volume integral equation (VIE) approach [28]. For a unit amplitude incident plane wave propagating along $\hat{\boldsymbol{u}}_{\mathrm{i}}$, the echo width is defined as

$$\sigma(-\hat{\boldsymbol{u}}_{\mathrm{i}}, \hat{\boldsymbol{u}}_{\mathrm{i}}) = 2\pi |F(\phi)|^2 \tag{72}$$

with ϕ the angle between the x-axis and $-\hat{\boldsymbol{u}}_{\mathrm{i}}$, and $F(\phi)$ the far field pattern, given by

$$F(\phi) = -\frac{\omega \mu_{\mathrm{e}}}{4} \sqrt{\frac{2j}{\pi k_{\mathrm{e}}}} \int\limits_{c} e^{j k_{\mathrm{e}} \hat{\boldsymbol{u}}_{\mathrm{i}} \cdot \boldsymbol{r}'} j_{s,z}(\boldsymbol{r}') \mathrm{d}c. \tag{73}$$

The results in Fig. 7 are normalized with respect to the wavelength λ_0 in the outside medium and plotted on a dB scale, i.e., we show the following quantity: $10 \log_{10} [\sigma(-\hat{\boldsymbol{u}}_{\mathrm{i}}, \hat{\boldsymbol{u}}_{\mathrm{i}})/\lambda_0]$. The first rectangular cylinder measures $1.8\lambda_0 \times 0.7\lambda_0$ and has material properties $\epsilon_{\mathrm{r}} = 2 - j$, $\mu_{\mathrm{r}} = 3 - 0.5j$. The horizontal and vertical sides of the rectangle are subdivided in 72 and 28 segments, resp., while 150 Fourier basis functions are considered in each direction. Its echo width is shown in Fig. 7a. The results in Fig. 7b belong to a $1.3\lambda_0 \times 0.03\lambda_0$ rectangular cylinder with relative permittivity $\epsilon_{\mathrm{r}} = 1.5 - 2j$ and relative permeability $\mu_{\mathrm{r}} = 5 - 3j$. The discretization is now performed using 130 and 3 segments on the horizontal and vertical sides, resp., again taking 150 Fourier basis functions into account. A very good agreement between the two methods is achieved, for both cases.

Next, we observe the tangential electric field and the radar cross-section (RCS), defined as $\sigma(\hat{\boldsymbol{u}}, \hat{\boldsymbol{u}}_{\mathrm{i}})$, where ϕ in (72) is now the angle between the x-axis and the direction of observation $\hat{\boldsymbol{u}}$, for a $1.5\,\mathrm{m} \times 1\,\mathrm{m}$ rectangular cylinder. The object has material properties $\epsilon_{\mathrm{r}} = 7$, $\mu_{\mathrm{r}} = 13$ and $\sigma = 0$, and is illuminated by a TM polarized plane wave at a frequency of 100 MHz, incident under a fixed angle of 30° with the x-axis, i.e., $\hat{\boldsymbol{u}}_{\mathrm{i}} = \frac{\sqrt{3}}{2}\hat{\boldsymbol{x}} + \frac{1}{2}\hat{\boldsymbol{y}}$ in (66). In this case, 200 sine functions are taken into account and the horizontal and vertical sides of the rectangle are discretized in 75 and 50 segments, resp. The results obtained by means of the proposed method are compared to a reference technique that employs a PMCHWT approach, with the same discretization. Fig. 8 shows a close agreement between both solutions. The position along the circumference of the rectangle is measured counterclockwise, starting from the bottom left corner.

In the above sections, we derived a DSA operator and BIE formalism for 2-D TM problems. Nonetheless, it should be remarked that we are also able to solve 2-D transverse electric (TE) problems, as the dielectric and magnetic contrast are both taken into account. It suffices to perform the appropriate substitutions:

$$e_z \to h_z \qquad \boldsymbol{h}_{\mathrm{t}} \to -\boldsymbol{e}_{\mathrm{t}} \qquad \epsilon_{\mathrm{r}} \to \mu_{\mathrm{r}} \qquad \mu_{\mathrm{r}} \to \epsilon_{\mathrm{r}}. \tag{74}$$

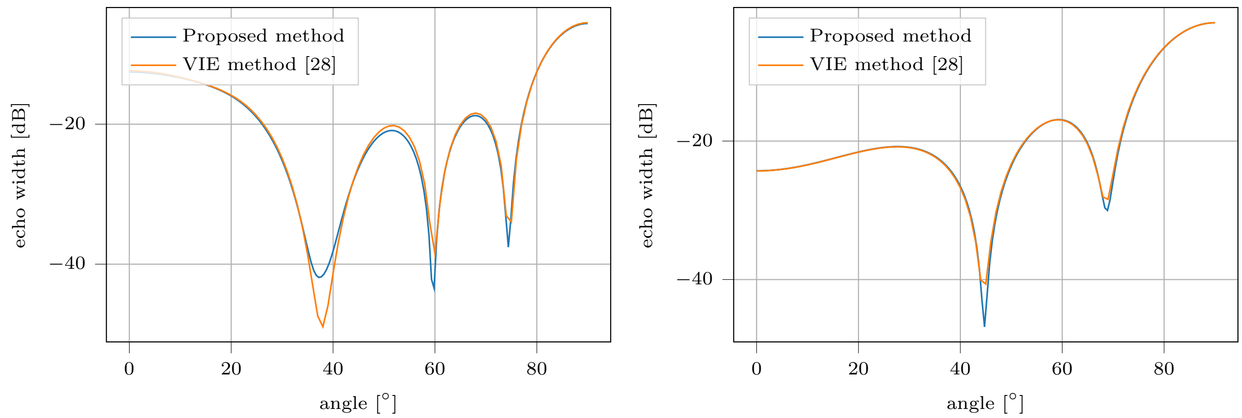

(a) $1.8\lambda_0 \times 0.7\lambda_0$, $\epsilon_\mathrm{r} = 2 - j$, $\mu_\mathrm{r} = 3 - 0.5j$

(b) $1.3\lambda_0 \times 0.03\lambda_0$, $\epsilon_\mathrm{r} = 1.5 - 2j$, $\mu_\mathrm{r} = 5 - 3j$

Figure 7: Echo width of a rectangular cylinder illuminated by a TM polarized plane wave. The reference solution is found by means of a VIE method [28].

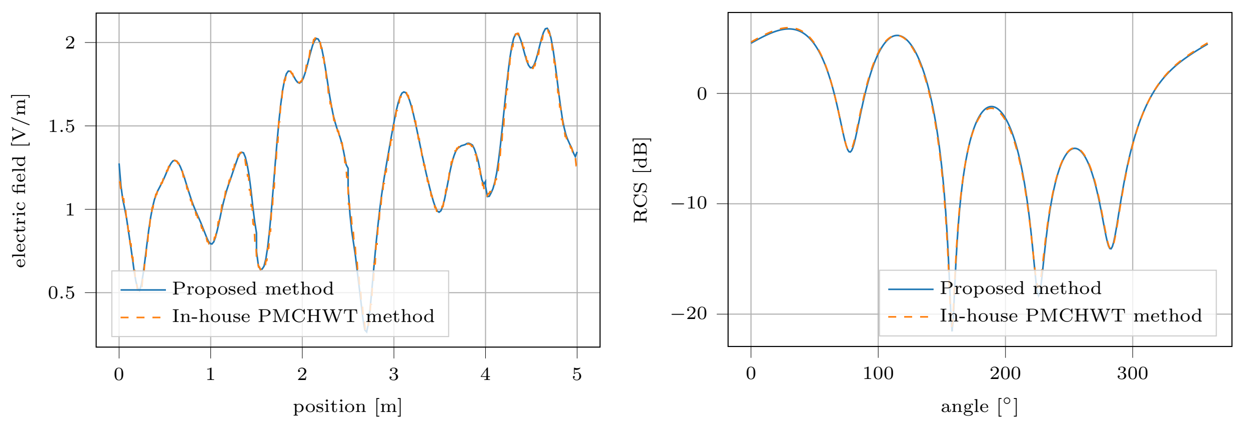

(a)

(b)

Figure 8: Magnitude of the tangential electric field at the boundary and radar cross-section of a $1.5\,\mathrm{m} \times 1\,\mathrm{m}$ rectangular cylinder with material properties $\epsilon_\mathrm{r} = 7$, $\mu_\mathrm{r} = 13$ and $\sigma = 0$, illuminated by a TM polarized plane wave at a frequency of 100 MHz, incident under an angle of 30° with the x-axis. The reference solution is found by means of a PMCHWT method.

Subsequently, we apply this strategy to study the echo width of the structure shown in Fig. 9: a thin perfectly electrically conducting (PEC) strip, covered by a layer of a lossless material exhibiting both dielectric ($\epsilon_\mathrm{r} = 2$) and magnetic ($\mu_\mathrm{r} = 2$) contrast, illuminated by a TE polarized plane wave. The results from our method are compared to those obtained via the coupled integral equations formulation in [29] and CST Studio Suite [30], again validating our advocated technique. When configuring CST's 3-D integral equations solver, the considered structure was modeled as a cuboid with an identical cross-section and a length $\ell = 2\lambda_0$. Thus, due care was taken to make the longitudinal dimension sufficiently long, limiting the effects of the end caps in the 3-D scenario. The results are therefore applicable to this 2-D example, provided an appropriate scaling factor is taken into account: $\sigma_{\text{3-D}} \approx \sigma_{\text{2-D}} \cdot 2\ell^2/\lambda_0$ [31].

Finally, we introduce the structure in Fig. 10a, which consists of a $0.75\lambda_0 \times 0.02\lambda_0$ PEC strip loaded by a $0.15\lambda_0 \times 0.15\lambda_0$ square with relative permittivity $\epsilon_\mathrm{r} = 4 - 4j$ and various relative permeabilities $\mu_\mathrm{r} \in \{1, 2, 5, 10\}$. The echo widths of this object under illumination by a TM polarized plane wave are shown in Fig. 10b. For the nonmagnetic case, the result is compared to the curve reported in [29].

To conclude this section, the required CPU time and memory usage of the Python implementation to determine the admittance matrix are reported in Table 1 for the example structures studied in this section, including the total number of edges involved in the discretization and the number of Fourier basis functions taken into account. Clearly, the computational requirements are very low and thus, the overall CPU time

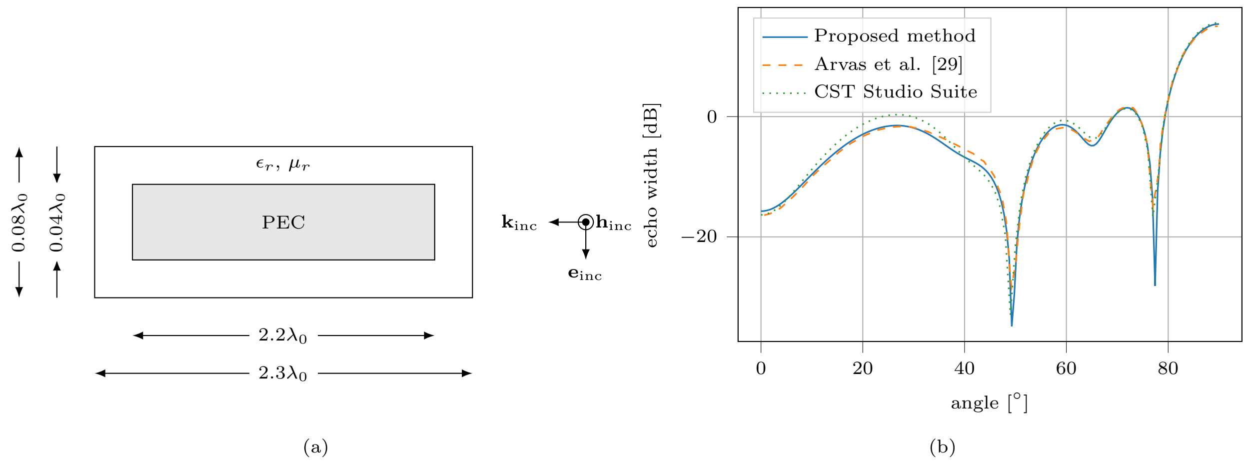

Figure 9: Echo width of a perfectly electrically conducting strip with dimensions $2.2\lambda_0 \times 0.04\lambda_0$ covered by a lossless medium with properties $\epsilon_r = 2$ and $\mu_r = 2$, resulting in total dimensions $2.3\lambda_0 \times 0.08\lambda_0$, under illumination by a TE polarized plane wave.

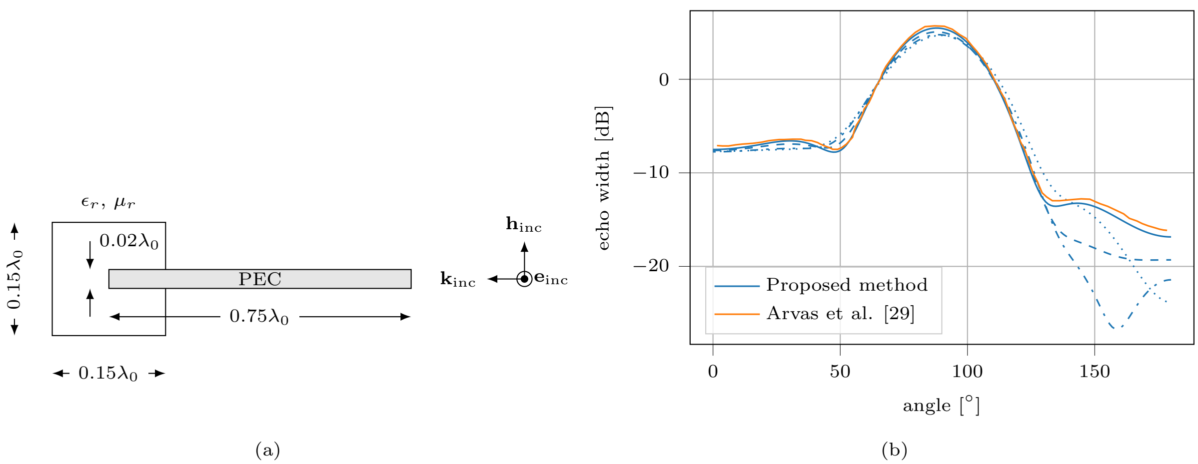

Figure 10: Echo width of a perfectly electrically conducting strip with dimensions $0.75\lambda_0 \times 0.02\lambda_0$ loaded by a square with side $0.15\lambda_0$ and material properties $\epsilon_r = 4 - 4j$ and $\mu_r \in \{1, 2, 5, 10\}$ (represented by solid, dashed, dash-dotted and dotted lines, resp.), under illumination by a TM polarized plane wave.

and memory usage are dominated by the implementation scheme of the BIE, which is a topic that has been abundantly treated in literature, e.g., [32].

5. Conclusion

In this paper, we presented a 2-D differential surface admittance technique to model electromagnetic scattering at circular and (combinations of) rectangular cylinders. In both cases, a Fourier series approach was used to construct the pertinent operator. The formulation in the Fourier domain was recast in a more appropriate form using constant and piecewise linear basis functions, allowing convenient combination with a boundary integral equations formalism. It was shown that special care needs to be taken to select this appropriate set of basis functions for the equivalent differential surface current density and tangential electric field, to obtain a fully convergent result for situations involving magnetic contrast. An analytical validation was performed for the case of circular cylinders and various numerical results further corroborated the precision and applicability of our method, both for circular and rectangular cylinders.

Example	# edges	# Fourier basis functions	*CPU time [s]*	*Memory usage [MiB]*
Fig. 7a	200	150	0.2	5.5
Fig. 7b	266	150	0.2	7.8
Fig. 8	250	200	0.3	7.7
Fig. 9	952	250	4.1	43.1
Fig. 10	484	250	2.6	12.2

Table 1: CPU timings and memory usage for the determination of the admittance matrix for the example structures studied in this section.

Appendix A. The Differential Surface Admittance Operator in the Fourier Domain

Appendix A.1. General Expression

We start from the general expression (B.1) and (B.2) for the longitudinal electric and azimuthal magnetic fields inside a circular cylinder. When we replace the material of the cylinder by the outside medium, i.e., we recreate the equivalent situation of Fig. 1b, these fields are given by

$$e_{z0} = \sum_n C_n J_n(k_\mathrm{e} r) e^{jn\phi}, \tag{A.1}$$

$$h_{\phi 0} = \frac{1}{j\omega\mu_\mathrm{e}} \frac{\mathrm{d}}{\mathrm{d}r} e_{z0} = \frac{k_\mathrm{e}}{j\omega\mu_\mathrm{e}} \sum_n C_n J_n'(k_\mathrm{e} r) e^{jn\phi}. \tag{A.2}$$

For the tangential electric field and the differential surface current density, we introduced Fourier series expansions (17) and (18), which we repeat here for convenience:

$$e_z = \sum_n \alpha_n e^{jn\phi} \qquad \text{and} \qquad j_{s,z} = \sum_n \iota_n e^{jn\phi}. \tag{A.3}$$

Now, we invoke the relations (1) and (2). In other words, we require that the electric field is identical at $r = a$ in both the original and equivalent situation and the surface current density is chosen such that the tangential magnetic field outside the cylinder remains unchanged. Imposing these conditions for each Fourier mode separately, leads to

$$\alpha_n = A_n J_n(k_\mathrm{i} a) = C_n J_n(k_\mathrm{e} a), \tag{A.4}$$

$$\iota_n = \frac{k_\mathrm{i}}{j\omega\mu_\mathrm{i}} A_n J_n'(k_\mathrm{i} a) - \frac{k_\mathrm{e}}{j\omega\mu_\mathrm{e}} C_n J_n'(k_\mathrm{e} a). \tag{A.5}$$

This finally results in an expression for the differential surface admittance operator Υ in the Fourier domain:

$$\iota_n = \left(\frac{k_\mathrm{i}}{j\omega\mu_\mathrm{i}} \frac{J_n'(k_\mathrm{i} a)}{J_n(k_\mathrm{i} a)} - \frac{k_\mathrm{e}}{j\omega\mu_\mathrm{e}} \frac{J_n'(k_\mathrm{e} a)}{J_n(k_\mathrm{e} a)} \right) \alpha_n \triangleq \Upsilon_n \alpha_n. \tag{A.6}$$

Appendix A.2. Limit for Large Values of n

The ratio between the Bessel function of order n and its derivative can be expressed as

$$\frac{J_n'(z)}{J_n(z)} = \frac{n J_n(z)/z - J_{n+1}(z)}{J_n(z)} = \frac{n}{z} - \frac{J_{n+1}(z)}{J_n(z)}. \tag{A.7}$$

Assuming $J_n(z) \neq 0$, we write the second term in (A.7) as a continued fraction [33]:

$$\frac{J_{n+1}(z)}{J_n(z)} = \cfrac{1}{2(n+1)z^{-1} - \cfrac{1}{2(n+2)z^{-1} - \cfrac{1}{2(n+3)z^{-1} - \dots}}} \qquad \text{for } z \neq 0, \tag{A.8}$$

such that

$$\lim_{n\to\infty}\frac{J_{n+1}(z)}{J_n(z)} \approx \frac{z}{2(n+1)} \tag{A.9}$$

and therefore

$$\lim_{n\to\infty}\frac{J'_n(z)}{J_n(z)} = \frac{n}{z} + \mathcal{O}\left(\frac{1}{n}\right). \tag{A.10}$$

Appendix B. Analytical Solution of the 2-D TM Plane Wave Scattering Problem for Circular Cylinders

In a 2-D TM context, the longitudinal electric field and the azimuthal magnetic field inside a cylinder can be represented in their most general form as

$$e_z = \sum_n A_n J_n(k_\mathrm{i} r)e^{jn\phi}, \tag{B.1}$$

$$h_\phi = \frac{1}{j\omega\mu_\mathrm{i}}\frac{\mathrm{d}}{\mathrm{d}r}e_z = \frac{k_\mathrm{i}}{j\omega\mu_\mathrm{i}}\sum_n A_n J'_n(k_\mathrm{i} r)e^{jn\phi}. \tag{B.2}$$

Outside the cylinder, on the other hand, we find the following expressions for the scattered fields:

$$e_{z,\mathrm{sc}} = \sum_n B_n H_n^{(2)}(k_\mathrm{e} r)e^{jn\phi}, \tag{B.3}$$

$$h_{\phi,\mathrm{sc}} = \frac{1}{j\omega\mu_\mathrm{e}}\frac{\mathrm{d}}{\mathrm{d}r}e_{z,\mathrm{sc}} = \frac{k_\mathrm{e}}{j\omega\mu_\mathrm{e}}\sum_n B_n H_n'^{(2)}(k_\mathrm{e} r)e^{jn\phi}, \tag{B.4}$$

where $H_n^{(2)}$ is the n-th order Hankel function of the second kind. As stated before, in (66), the incident fields are given by

$$e_{z,\mathrm{inc}} = \sum_n j^{-n} J_n(k_\mathrm{e} r)e^{jn\phi}, \tag{B.5}$$

$$h_{\phi,\mathrm{inc}} = \frac{1}{j\omega\mu_\mathrm{e}}\frac{\mathrm{d}}{\mathrm{d}r}e_{z,\mathrm{inc}} = \frac{k_\mathrm{e}}{j\omega\mu_\mathrm{e}}\sum_n j^{-n} J'_n(k_\mathrm{e} r)e^{jn\phi}. \tag{B.6}$$

Imposing the continuity of the total tangential electric and magnetic fields for every mode at the boundary $\mathcal{C}$ of the cylinder, i.e., $e_z = e_{z,\mathrm{inc}} + e_{z,\mathrm{sc}}$ and $h_\phi = h_{\phi,\mathrm{inc}} + h_{\phi,\mathrm{sc}}$ for $r = a$, finally leads to

$$A_n = \frac{1}{\xi}\left(j^{-n}\frac{k_\mathrm{e}}{j\omega\mu_\mathrm{e}}\frac{2j}{\pi k_\mathrm{e} a}\right), \tag{B.7}$$

$$B_n = \frac{j^{-n}}{\xi}\left(\frac{k_\mathrm{e}}{j\omega\mu_\mathrm{e}}J'_n(k_\mathrm{e} a)J_n(k_\mathrm{i} a) - \frac{k_\mathrm{i}}{j\omega\mu_\mathrm{i}}J_n(k_\mathrm{e} a)J'_n(k_\mathrm{i} a)\right), \tag{B.8}$$

with

$$\xi = -\frac{k_\mathrm{e}}{j\omega\mu_\mathrm{e}}J_n(k_\mathrm{i} a)H_n'^{(2)}(k_\mathrm{e} a) + \frac{k_\mathrm{i}}{j\omega\mu_\mathrm{i}}J'_n(k_\mathrm{i} a)H_n^{(2)}(k_\mathrm{e} a). \tag{B.9}$$

By means of these results, we can directly compare the numerically calculated Fourier coefficients to their analytical counterparts, which we will denote with a tilde ($\tilde{\cdot}$): $\tilde{\alpha}_n = A_n J_n(k_\mathrm{i} a)$ and $\tilde{\iota}_n = \Upsilon_n \tilde{\alpha}_n$ (A.6).

Appendix C. Term-by-Term Differentiation

We assume that the total tangential electric field $e_z(x, y)$ is at least twice continuously differentiable with respect to y for all $y \in [0, l_y]$, with x fixed to 0 or l_x, and expand its odd periodic extension in a Fourier sine series:

$$e_z(x, y) = \sum_n \alpha_n(y)\sin\frac{n\pi x}{l_x} \qquad \text{with } \alpha_n(y) = \frac{1}{l_x}\int_{-l_x}^{l_x} e_z(x, y)\sin\frac{n\pi x}{l_x}\,\mathrm{d}x\,. \tag{C.1}$$

Now, we calculate the second-order derivative of the Fourier coefficients with respect to y. Given the aforementioned differentiability properties of e_z, we can invoke Leibniz' integral rule and find

$$\frac{\mathrm{d}^2\alpha_n}{\mathrm{d}y^2} = \frac{\mathrm{d}^2}{\mathrm{d}y^2}\left[\frac{1}{l_x}\int_{-l_x}^{l_x} e_z(x,y)\sin\frac{n\pi x}{l_x}\,\mathrm{d}x\right] = \frac{1}{l_x}\int_{-l_x}^{l_x}\frac{\partial^2 e_z}{\partial y^2}\sin\frac{n\pi x}{l_x}\,\mathrm{d}x\,, \tag{C.2}$$

which is the expression for the Fourier sine coefficients of $\frac{\partial^2 e_z}{\partial y^2}$. Imposing $\left.\frac{\partial^2 e_z}{\partial y^2}\right|_{x=0} = \left.\frac{\partial^2 e_z}{\partial y^2}\right|_{x=l_x} = 0$, we can state that

$$\frac{\partial^2 e_z}{\partial y^2} = \sum_n \frac{\mathrm{d}^2\alpha_n}{\mathrm{d}y^2}\sin\frac{n\pi x}{l_x}, \tag{C.3}$$

or, the second order partial derivative of the total tangential electric field Fourier series with respect to y can be evaluated term by term.

Now, we assume that the total tangential electric field $e_z(x,y)$ is at least twice continuously differentiable with respect to x as well, for all $x \in [0, l_x]$, with y fixed to 0 or l_y, and invoke a combination of the following theorems [34]:

Theorem 1. *Suppose $f(x)$ is a continuous function, its derivative $f'(x)$ is piecewise smooth and $f(0) = f(L) = 0$, then the Fourier sine series can be differentiated term by term and the result is the Fourier cosine series of the derivative.*

Theorem 2. *Suppose $f(x)$ is a continuous function and its derivative $f'(x)$ is piecewise smooth, then the Fourier cosine series can be differentiated term by term and the result is the Fourier sine series of the derivative.*

We then find that the second order partial derivative of the total tangential electric field Fourier series with respect to x can also be evaluated term by term.

References

[1] A. Poggio, E. Miller, Integral Equation Solutions of Three-dimensional Scattering Problems, Pergamon, New York, 1973, Ch. 4, pp. 159–264.

[2] M. Chari, Z. Csendes, Finite element analysis of the skin effect in current carrying conductors, IEEE Transactions on Magnetics 13 (5) (1977) 1125–1127. doi:10.1109/TMAG.1977.1059545.

[3] G. Costache, Finite element method applied to skin-effect problems in strip transmission lines, IEEE Transactions on Microwave Theory and Techniques 35 (11) (1987) 1009–1013. doi:10.1109/TMTT.1987.1133799.

[4] R.-B. Wu, J.-C. Yang, Boundary integral equation formulation of skin effect problems in multiconductor transmission lines, IEEE Transactions on Magnetics 25 (4) (1989) 3013–3015. doi:10.1109/20.34354.

[5] K. Coperich, A. Ruehli, A. Cangellaris, Enhanced skin effect for partial-element equivalent-circuit (PEEC) models, IEEE Transactions on Microwave Theory and Techniques 48 (9) (2000) 1435–1442. doi:10.1109/22.868992.

[6] L. Medgyesi-Mitschang, J. Putnam, Integral equation formulations for imperfectly conducting scatterers, IEEE Transactions on Antennas and Propagation 33 (2) (1985) 206–214. doi:10.1109/TAP.1985.1143560.

[7] M. Al-Qedra, J. Aronsson, V. Okhmatovski, A novel skin-effect based surface impedance formulation for broadband modeling of 3-D interconnects with electric field integral equation, IEEE Transactions on Microwave Theory and Techniques 58 (12) (2010) 3872–3881. doi:10.1109/TMTT.2010.2087350.

[8] D.-S. Wang, Limits and validity of the impedance boundary condition on penetrable surfaces, IEEE Transactions on Antennas and Propagation 35 (4) (1987) 453–457. doi:10.1109/TAP.1987.1144125.

[9] D. De Zutter, L. Knockaert, Skin effect modeling based on a differential surface admittance operator, IEEE Transactions on Microwave Theory and Techniques 53 (8) (2005) 2526–2538. doi:10.1109/TMTT.2005.852766.

[10] J. Peeters, I. Bogaert, D. De Zutter, Calculation of MoM interaction integrals in highly conductive media, IEEE Transactions on Antennas and Propagation 60 (2) (2012) 930–940. doi:10.1109/TAP.2011.2173105.

[11] H. Rogier, D. De Zutter, L. Knockaert, Two-dimensional transverse magnetic scattering using an exact surface admittance operator, Radio Science 42 (3) (2007). doi:10.1029/2006RS003516.

[12] T. Demeester, D. De Zutter, Quasi-TM transmission line parameters of coupled lossy lines based on the Dirichlet to Neumann boundary operator, IEEE Transactions on Microwave Theory and Techniques 56 (7) (2008) 1649–1660. doi:10.1109/TMTT.2008.925215.

[13] T. Demeester, D. De Zutter, Construction of the Dirichlet to Neumann boundary operator for triangles and applications in the analysis of polygonal conductors, IEEE Transactions on Microwave Theory and Techniques 58 (1) (2010) 116–127. doi:10.1109/TMTT.2009.2035881.

[14] M. Huynen, M. Gossye, D. De Zutter, D. Vande Ginste, A 3-D differential surface admittance operator for lossy dipole antenna analysis, IEEE Antennas and Wireless Propagation Letters 16 (2017) 1052–1055. doi:10.1109/LAWP.2016.2619558.

[15] M. Huynen, D. De Zutter, D. Vande Ginste, Rigorous full-wave resistance and inductance computation of 3-D interconnects, IEEE Microwave and Wireless Components Letters 28 (6) (2018) 455–457. doi:10.1109/LMWC.2018.2825652.

[16] M. Huynen, K. Y. Kapusuz, X. Sun, G. Van der Plas, E. Beyne, D. De Zutter, D. Vande Ginste, Entire domain basis function expansion of the differential surface admittance for efficient broadband characterization of lossy interconnects, IEEE Transactions on Microwave Theory and Techniques 68 (4) (2020) 1217–1233. doi:10.1109/TMTT.2019.2957485.

[17] U. R. Patel, B. Gustavsen, P. Triverio, An equivalent surface current approach for the computation of the series impedance of power cables with inclusion of skin and proximity effects, IEEE Transactions on Power Delivery 28 (4) (2013) 2474–2482. doi:10.1109/TPWRD.2013.2267098.

[18] U. R. Patel, B. Gustavsen, P. Triverio, Proximity-aware calculation of cable series impedance for systems of solid and hollow conductors, IEEE Transactions on Power Delivery 29 (5) (2014) 2101–2109. doi:10.1109/TPWRD.2014.2330994.

[19] U. R. Patel, P. Triverio, MoM-SO: A complete method for computing the impedance of cable systems including skin, proximity, and ground return effects, IEEE Transactions on Power Delivery 30 (5) (2015) 2110–2118. doi:10.1109/TPWRD.2014.2378594.

[20] U. R. Patel, P. Triverio, Accurate impedance calculation for underground and submarine power cables using MoM-SO and a multilayer ground model, IEEE Transactions on Power Delivery 31 (3) (2016) 1233–1241. doi:10.1109/TPWRD.2015.2469599.

[21] U. R. Patel, P. Triverio, Skin effect modeling in conductors of arbitrary shape through a surface admittance operator and the contour integral method, IEEE Transactions on Microwave Theory and Techniques 64 (9) (2016) 2708–2717. doi:10.1109/TMTT.2016.2593721.

[22] U. R. Patel, P. Triverio, S. V. Hum, A novel single-source surface integral method to compute scattering from dielectric objects, IEEE Antennas and Wireless Propagation Letters 16 (2017) 1715–1718. doi:10.1109/LAWP.2017.2669183.

[23] P. Ylä-Oijala, S. P. Kiminki, Challenges in developing efficient Calderón preconditioners for resonating or high material contrast penetrable objects, Journal of Computational and Applied Mathematics 289 (2015) 296–305. doi:10.1016/j.cam.2015.01.005.

[24] M. Gossye, M. Huynen, D. Vande Ginste, D. De Zutter, H. Rogier, A Calderón preconditioner for high dielectric contrast media, IEEE Transactions on Antennas and Propagation 66 (2) (2018) 808–818. doi:10.1109/TAP.2017.2778014.

[25] M. Gossye, D. Vande Ginste, H. Rogier, Electromagnetic modeling of high magnetic contrast media using Calderón preconditioning, Computers and Mathematics with Applications 77 (6) (2019) 1626–1638. doi:10.1016/J.CAMWA.2018.08.045.

[26] C. Balanis, Advanced Engineering Electromagnetics, 2nd Edition, John Wiley & Sons, New Jersey, 2012, Ch. 7, pp. 328–331.

[27] M. S. Tong, W. C. Chew, The Nyström Method in Electromagnetics, John Wiley & Sons, Singapore, 2020.

[28] J. Jin, V. V. Liepa, C. Tai, A volume-surface integral equation for electromagnetic scattering by inhomogeneous cylinders, Journal of Electromagnetic Waves and Applications 2 (5/6) (1988) 573–588. doi:10.1163/156939388X00170.

[29] E. Arvas, T. K. Sarkar, RCS of two-dimensional structures consisting of both dielectrics and conductors of arbitrary cross section, IEEE Transactions on Antennas and Propagation 37 (5) (1989) 546–554. doi:10.1109/8.24182.

[30] Dassault Systèmes, CST Studio Suite 3D EM simulation and analysis software (2020).
URL `https://www.3ds.com/products-services/simulia/products/cst-studio-suite/`

[31] C. Balanis, Advanced Engineering Electromagnetics, 2nd Edition, John Wiley & Sons, New Jersey, 2012, Ch. 11, p. 584.

[32] W. C. Chew, J.-M. Jin, E. Michielssen, J. Song (Eds.), Fast and Efficient Algorithms in Computational Electromagnetics, Artech House, Boston, 2001.

[33] A. Cuyt, V. B. Petersen, B. Verdonk, H. Waadeland, W. B. Jones, Handbook of Continued Fractions for Special Functions, Springer, New York, 2008, pp. 349–356.

[34] R. Haberman, Elementary Applied Partial Differential Equations with Fourier Series and Boundary Value Problems, 2nd Edition, Prentice Hall, New Jersey, 1987, Ch. 3, pp. 100–106.